Effect of mechanical milling on the harmonic structure development during spark plasma sintering of Ti-5Al-2Sn-4Zr-4Mo-2Cr-1Fe β-metastable titanium alloy (β-Cez alloy)

Bhupendra Sharma, Benoît Denand, Petr Harcuba, Guillaume Geandier, Kei Ameyama, Guy Dirras, Elisabeth Aeby-Gautier

Version of Record: https://www.sciencedirect.com/science/article/pii/S0925838820348465
Manuscript_c12bcc387727e5ea24132a3deae4d883

Effect of mechanical milling on the harmonic structure development during spark plasma sintering of Ti-5Al-2Sn-4Zr-4Mo-2Cr-1Fe β-metastable titanium alloy (β-Cez alloy)

Bhupendra Sharma[a,b], *Benoît Denand[a], Petr Harcuba[a,c], Guillaume Geandier[a], Kei Ameyama[b], Guy Dirras[d], Elisabeth Aeby-Gautier[a],*

[a] Institut Jean Lamour, UMR 7198, CNRS—Université de Lorraine, Campus ARTEM, 2 allée André Guinier BP 50840, 54011 Nancy CEDEX, France;
[b] Department of Mechanical Engineering, Faculty of Science and Engineering, Ritsumeikan University, Kusatsu 525-8577, Japan
[c] Department of Physics of Materials, Charles University, Ke Karlovu 5, 12116, Prague, Czech Republic
[d] Université Paris 13, Sorbonne Paris-Cité, 99 Avenue Jean-Baptiste Clément, 93430 Villetaneuse, France

Abstract

The present study focuses on the formation of harmonic microstructures in a metastable β titanium alloy, the β-Cez alloy (Ti-5Al-2Sn-4Zr-4Mo-2Cr-1Fe – T_β = 895°C). Previous studies emphasized mainly fabrication and improvements in the mechanical properties of alloys prepared by powder metallurgy and showing a harmonic structure. In this study, the harmonic structure was obtained after mechanical milling of the initial powder, followed by a Spark Plasma Sintering (SPS) process. During the process, phase transformations occur that are dependent on the initial state of the powder. Moreover, their kinetics depend on the thermo-mechanical history of the powder. In order to analyze the microstructure formation, the behavior of milled and non-milled powders was studied during a heat treatment similar to the one applied during the SPS process. In-situ high-energy X-ray diffraction was used to characterize the evolution of phases during the thermal treatment. Additional in situ electrical resistivity measurements were carried out on sintered compact specimens. Characterizations evidenced that the initial powder is in a β metastable state. After mechanical milling, stress/strain induced α" martensite was observed inside the powder's β grains. The stepwise microstructural characterization revealed the influence of the initial state of the mechanically milled powder on the formation of a harmonic α arrangement in the β matrix consisting of nodular α grains in the powder shell and α lamellae in the powder core. The stress/strain induced martensite formed during the milling associated with the heavier deformation at the powder surface areas contributes highly to the formation of an arrangement of nodular α grains by a recovery/recrystallization phenomenon of β and α"/α phases during the heating.

Keywords: β-metastable titanium alloys; harmonic structures; powder metallurgy; in-situ synchrotron X-ray diffraction; phase transformations.

1. Introduction

The β-metastable titanium alloys are a particular class of titanium alloys having great potential to use in versatile applications, such as aerospace, automotive, and biomedical applications, owing to their outstanding chemical and mechanical properties [1-5]. In such typical engineering applications, an appropriate balance of strength and ductility is required simultaneously. Nonetheless, from a conventional grain boundary strengthening point of view, these properties are considered as antinomies [6-7]. However, comprehensive research efforts are being made for improving mechanical properties to enhance the reliability of performance. Recent studies have shown that a blend of fine and coarse grain size distribution in the microstructure matrix is very effective in achieving an attractive combination of high strength and acceptable ductility [8-9]. In particular, Ameyama and co-authors [10] proposed an elegant microstructural design, called "harmonic structure," which is essentially a bimodal microstructure wherein the coarse-grained areas ("core") are present as embedded islands in the matrix of the three-dimensional continuously connected network ("shell") of fine-grained areas. The concept of harmonic structure design has been successfully applied in a variety

of materials such as Co-Cr-Mo alloy [10], Ti-6Al-4V [11], and SUS304L [12] steel, Cp-Ti [13], and Ti-Al [14] alloys. All the harmonic microstructure designed materials demonstrated a significantly better performance [15-17] as compared to their homogeneous fine or coarse-grained counterparts [18]. However, until now, most of the studies were focused on the various fabrication processes and their corresponding mechanical properties, and no detailed studies of phase and microstructure evolutions, during the fabrication of harmonic structure materials, have been reported. Hence, it appears clear that investigating the microstructure evolutions that occur during the process are key steps for their design and to reach controlled microstructures with some desired properties (the function of size, fraction of shell and core phases). Moreover, in the case of Ti alloys, studies were realized on Cp-Ti alloys and Ti6Al4V. For both cases, the β phase formed during solidification in the powders transforms on cooling in α or α' martensite. In the case of β-metastable titanium alloys, the β phase is expected to remain in a metastable state after the powders' rapid cooling. Differences in the phase transformation sequences are thus expected as compared to Cp-Ti or Ti6Al4V alloys. Indeed, Grosdidier and co-authors [19] have shown that stress/strain-induced martensite is formed during deformation of β-metastable phase at room temperature, in β-Cez alloy. Such behavior may thus occur during milling. In consequence, the phase transformation sequences during the SPS treatment may differ with milling or without milling.

In the present paper we focus on the microstructure and phase evolutions occurring during the processing of the β-Cez Ti powders in order to describe the phenomena involved in each step. In situ high-energy X-ray diffraction (HEXRD) and electrical resistivity [20-21], were used to reach the nature of the phases and their evolutions during the thermal treatment of Initial Powder (IP) and Mechanical Milled (MM) powders and on as-sintered specimens. In addition, scanning electron microscopy with EDX, EBSD analysis and transmission electron microscopy were used to characterize the microstructures.

2. Materials and Experimental setup

The initial material of Plasma Rotating Electrode Processed (PREP) [22-23] β-Cez powder was obtained from Fukuda Company. The initial powder had an average particle size of 150 µm. Its chemical composition is given in **Table 1**. The PREP process is considered most suitable for preparing high quality powders of very reactive metals such as Titanium [11]. A part of the initial powder (IP) was mechanically milled (MM) in a planetary ball mill using steel vials filled with argon gas and steel balls. The milling was carried out at a rotation speed of 200 rpm for 25 hours.

Table 1. The nominal composition of the β-Cez Ti alloy used in this study.

Elements	Al	Mo	Cr	Zr	Sn	Fe	O	N	C	Ti
Mass%	5	4	2	4	2	1	1055 (ppm)	59 (ppm)	52 (ppm)	Bal.

To obtain dense specimens, IP and MM powders were sintered by spark plasma sintering (SPS) using graphite die and punch. The heat treatment shown in **Fig. 1b** was realized under argon gas. It consisted in a heating at 0.8 °C/s up to 800 °C, a dwell for 30 min at that temperature, followed by a cooling at 0.23 °C/s. A 50 MPa pressure was simultaneously applied to reduce porosities in the sample (**Fig. 1a**). It would be worth to mention that the real temperature attained in the powder during spark plasma sintering is approximately 50 °C higher than the preset and measured temperature depending on the method of temperature measurement and dimensions of the die used for powder consolidation [11]. Therefore, setting the sintering temperature at approximately 800 °C appears to be reasonable to make sure that the sintering is carried out well below β transus temperature defined at about 895 °C [24].
The sintered specimens, prepared from initial powder and mechanical milled powder, will be referred to as IP-SPS and MM-SPS specimens in the later sections of this manuscript.

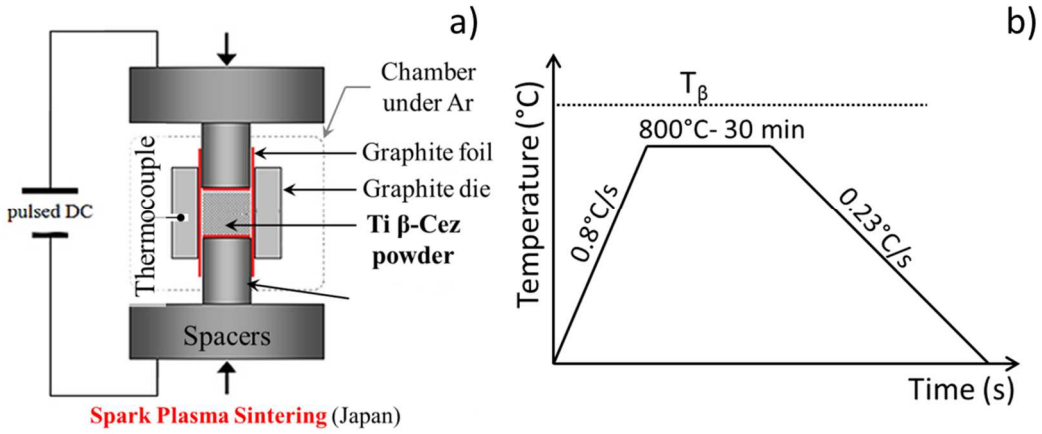

Fig. 1. a) The SPS process description and b) Thermal treatment during the SPS process.

During the processing of the powders, some contamination by oxygen or carbon could occur. Any contamination will change the chemical composition of the powders, and in consequence the transus temperature T_β. Such behavior was observed when processing Ti6Al4V-TiB composite [25]. In order to check the occurrence of any contamination, the transus temperature T_β of IP-SPS and MM-SPS specimens was characterized using electrical resistivity. The result given in section 3.2 shows that the T_β temperature of the specimens was the same as that of the initial rod.

The phase transformation kinetics was studied by in-situ HEXRD. The HEXRD experiments were performed at the European Synchrotron Radiation Facility (ESRF) in Grenoble, France, on the ID15A beamline. The radiation used was a high energy X-ray synchrotron radiation with a monochromatic beam of 90 keV ($\lambda = 0.13776\ A^{\circ}$). The beam size was 400 x 400 μm^2. A DECTRIS Pilatus image plate detector (pixel size 172 μm) with CdTe sensor material placed at 0.7 m from the sample allowed the collection of the complete Debye–Scherrer rings in the 2θ range 2 - 9°. The high photon flux gives a high-quality diffraction signal. A rapid recording of 2D Debye Scherrer diffraction patterns can thus be obtained [26]. Considering the heating and cooling rates involved (Fig 1), the HEXRD frames were recorded with one frame rate per second (i.e. one frame per 0.8°C during heating and one frame per 0.23 °C on cooling). Using this method, we could follow the successive evolution of Debye–Scherrer rings during the thermal treatment.
After experiment, each 2D diffraction pattern was analyzed. At first, data integration was processed using PyFAI software to convert the 2D images to classical 1D diffractograms [27]. Each diffraction diagram was analyzed using the multiphase Rietveld refinement with the software FullProf [26][28] to get different results as the nature and amount of phases.
For the HEXRD experiments, the IP and MM powders were considered. The powders were inserted in a capillary tube with a S-type thermocouple. The thermocouple was positioned close to the X-ray beam path in order to accurately control the temperature assessment during patterns acquisition. The capillary was placed at the center of an in-house made radiant furnace [29] on a sample holder with a rotating platform. To obtain good counting statistics by increasing the number of particles analyzed, a rotation of the quartz capillary was applied at one complete rotation per second. The capillary was inside a quartz chamber where an argon gas flow circulated in order to limit powder oxidation during the thermal path. The thermocouple placed in the capillary was used to measure and control the temperature using a 3508 Eurotherm controller. The thermal treatment applied during experiments was similar to the one used during the SPS treatment shown **Fig. 1b**.
In order to analyze any possible oxygen or nitrogen contamination, electrical resistivity measurements were performed on dense SPS specimens using a four point's method [30]. After SPS treatment, specimens were machined in cylinders, 3.8 mm in diameter and 20 mm in length. This same method was used to check the possible precipitation during heating for a IP-SPS specimen in a β-metastable initial state. The machined IP-SPS sample was first heated up to 920 °C, in the β temperature range

and further quenched in order to obtain a β-metastable phase, with equiaxed β grains. The electrical resistivity measurements were performed with the heat treatment given in **Fig 1b** .

Microstructure characterizations were realized on powders as well as on dense specimens. For dense specimens obtained by SPS, the microstructures were observed in the transverse direction. Powders microstructure characterizations were realized on powders embedded in copper resins. Microstructural observations were realized after using polishing paper grit until size 4000. The final polishing of the samples (specimens and powders) was performed with a mixture of colloidal silica (OP-S) and Hydrogen Peroxide (H_2O_2) (25%) solution. For finer scale microstructural characterizations, the thin foils have been prepared using a FEI Helios NanoLab 600i DualBeam (FEI brand) equipped with the Focused Ion Beam (FIB) technique. This operation consist of successive steps: a protective deposit of platinum assisted by electrons is carried out (220 nm thickness) then by Ga ions (2 µm final thickness). A slice is making and then thinning to obtain a 1.5 µm thick foil. Then it comes an operation of cutting the foil's contours and welding on the micromanipulator. The foil is then extracted from the bulk to be welded on the grid. The final thinning is gotten by using a voltage of 30kV and gradually descending to a voltage of 1kV to obtain a foil 80-100nm thick.
The observations were realized by SEM using a Quanta 650 FEG (FEI brand) and a Gemini500 FEG (Zeiss brand) for morphology analyses, EDX for chemical analysis and EBSD maps (Oxford Instruments). The electron beam energy (kV) was chosen between 5 and 15 kV for Back Scattering Electron (BSE) observations and between 15 to 20 kV for EBSD maps. To characterize the microstructure and grain morphologies evolution, several thermal treatments were performed and interrupted by helium gas quenching at 450 °C, 600 °C, 800 °C without holding, and 800 °C with a holding of 30 min. TEM observations of MM powder were realized using an ACCELARM-200F FEG (JEOL Brand).

3. Results and Discussion

3.1. Characterizations of IP and MM powders

Characterizations of the as received IP and MM powders reveal significant differences in the crystallographic structures and microstructures.
HEXRD diffraction diagrams given in **Fig. 2** highlight the major difference. For the IP powder, diffraction peaks correspond to those of the BCC β phase (**Fig. 2a**). A little peak close to $(110)_\beta$ indicates the presence of α phase (zoom on Fig. 2a and more visible on Fig. 8a), which amount can be estimated at about 1 wt%. Concerning the MM powder (Fig 2b), much more diffraction peaks can be observed. The refinement of the diffraction diagram leads to a mixture of BCC β phase and orthorhombic α" phase. The amount of α" phase is 73 wt.%.

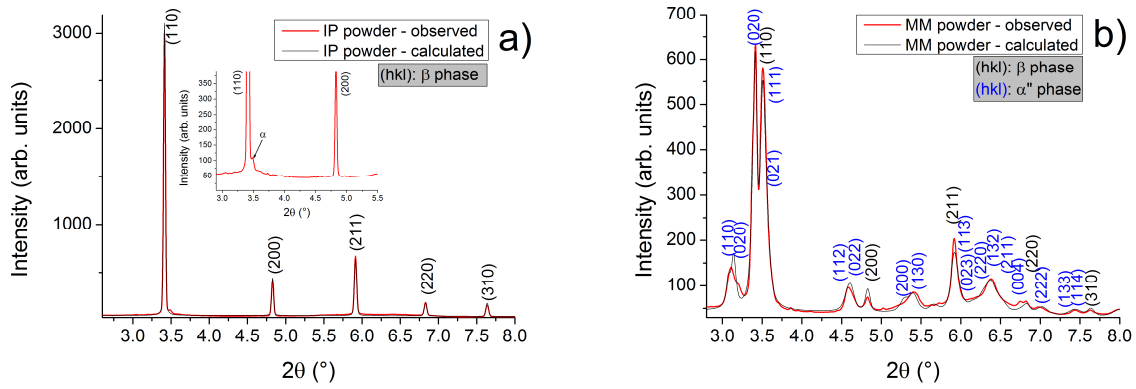

Fig. 2: HEXRD diffractograms of a) IP powder and b) MM powder.

These results are the ones expected considering the literature. Indeed, the powder processing involves very rapid cooling. For the β-Cez alloy, such rapid cooling avoids the phase transformations of the β

phase below the β transus temperature [31]. Thus, a resulting β metastable state is obtained in the IP powder. It should be noted that TEM studies in the literature report the presence of ω_{ath} [31-32] after quenching from above the β transus temperature. This ω_{ath} phase could be expected but is not evidenced by HEXRD, certainly due to its very low size. The presence of orthorhombic martensite in the MM powder evidence a strong modification during milling. The β-metastable phase is partially transformed in stress/strain induced α" martensite. This result can also be related to previous studies on bulk specimens of β-Cez alloy. Indeed, the formation of stress/strain-induced martensite during tensile tests of specimens in a β-metastable state was reported in [19].

Fig. 3 shows the morphology and particle size of the IP β-Cez powder. It can be seen that the powder particles are spherical (**Fig. 3a**) and have a wide size distribution, between 100 µm and 200 µm. The typical microstructure of the IP powder, obtained at a higher magnification, is shown in **Fig. 3b**. Different β grains can be observed, in which chemical segregation, associated with the dendritic microstructure formed during solidification, is identified [14] (**Fig. 3b**). The segregations in the β phase reveals bright zones, characterized by an enrichment in Zr, Cr and Fe and a depletion in Mo (**Fig. 3c and 3d**). Those segregations can also be observed in **Fig 3b**. It can also be mentioned that one powder particle in **Fig 3a** does not highlight any segregation nor internal grain structure. This could be associated to a very rapid cooling of that powder grains. Moreover, some porosities are observed and the presence of α or α" was not clearly evidenced, confirming the HEXRD result.

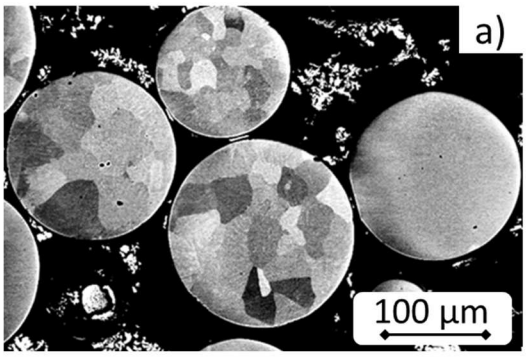

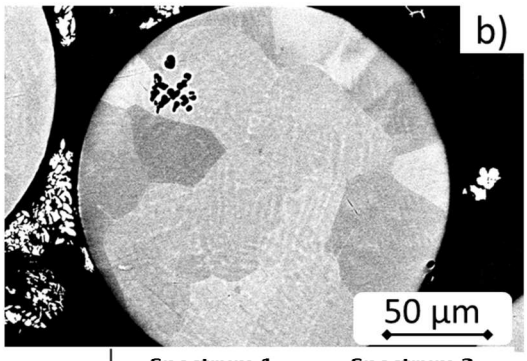

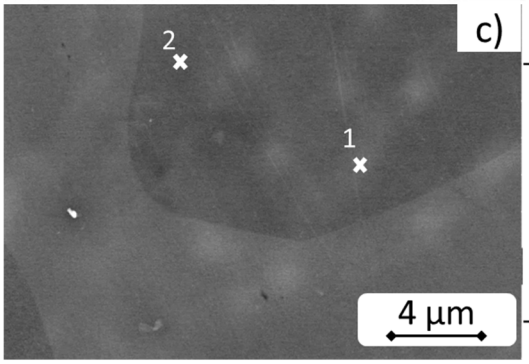

d)

Element	Spectrum 1 (wt. %)	Spectrum 2 (wt. %)
Al	4.3	4.4
Cr	**2.6**	**1.9**
Fe	**1.4**	**1.0**
Zr	**5.2**	**3.6**
Mo	**3.1**	**4.0**
Sn	1.9	2.0
Ti	81.5	83.1
Total:	100.00	100.00

Fig. 3. Representative SEM-BSE micrographs of IP powder a) overview magnification, b) particle with local segregations and pores, c) detail of chemical segregation, d) EDX characterization realized on white spot (spectrum 1) and matrix (spectrum 2) on the micrograph c).

The microstructure of the MM powder is illustrated in **Fig. 4**. Observations at the lower magnification (**Fig. 4a**), highlight a deformation of the powders for almost all particles. Chemical micro-segregations with a dendritic morphology are still observed as well as a few porosities. At higher magnification, parallel plates are evidenced, at the surface and inner part the MM powder particles (**Fig. 4b and 4c**), corresponding to the strain-induced martensite. Near the surface, a layer of about 7 (± 2.4) µm can be noticed, in which the distance between the dendritic arms is reduced (**Fig. 4d**). A higher deformation due to the milling can thus be associated with the lower inter-dendritic distance. Observations at higher magnification by SEM (**Fig. 4b and d**) and TEM (**Fig. 5**) reveal differences at the surface and interior of the powder particle. The morphology of the α" observed in the inner part of the powder

particle is clearly acicular, with plates having a similar morphologic orientation while it is finer and more block-like in shape at the surface (**Fig. 4c and Fig. 5**), and of which the orientation is no more well identified.

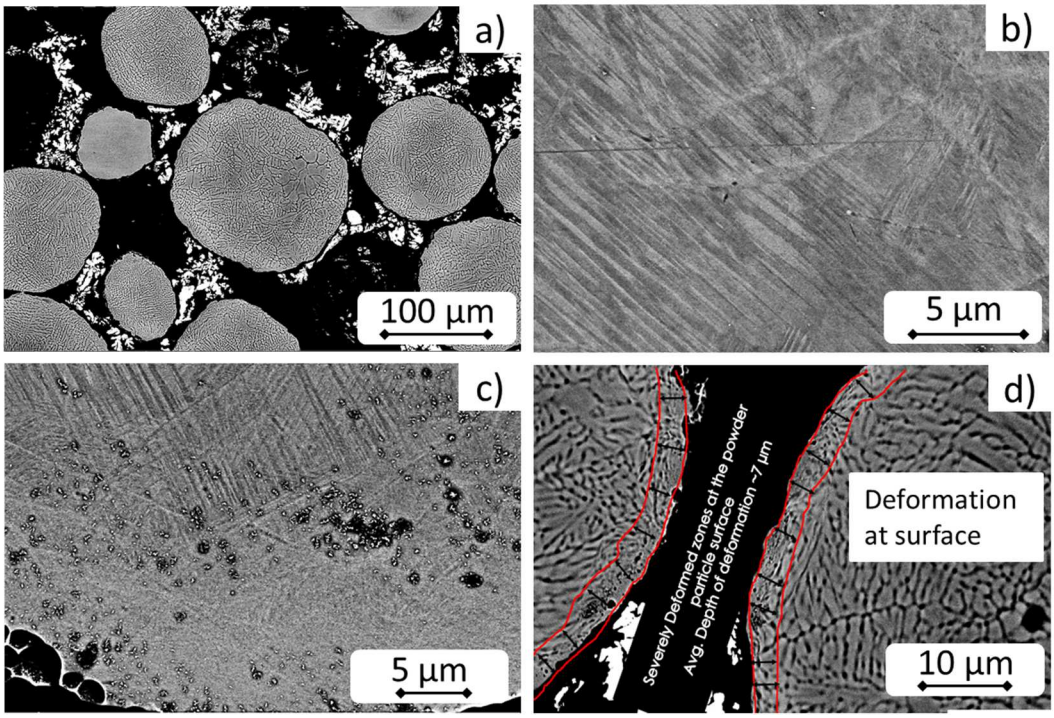

Fig. 4. Representative SEM-BSE micrographs of mechanically milled powder a) overview magnification, b) detail of inner part of the particle, c) detail of surface of the particle presenting stress-induced martensite and d) plastically deformed area at the powder particle surface.

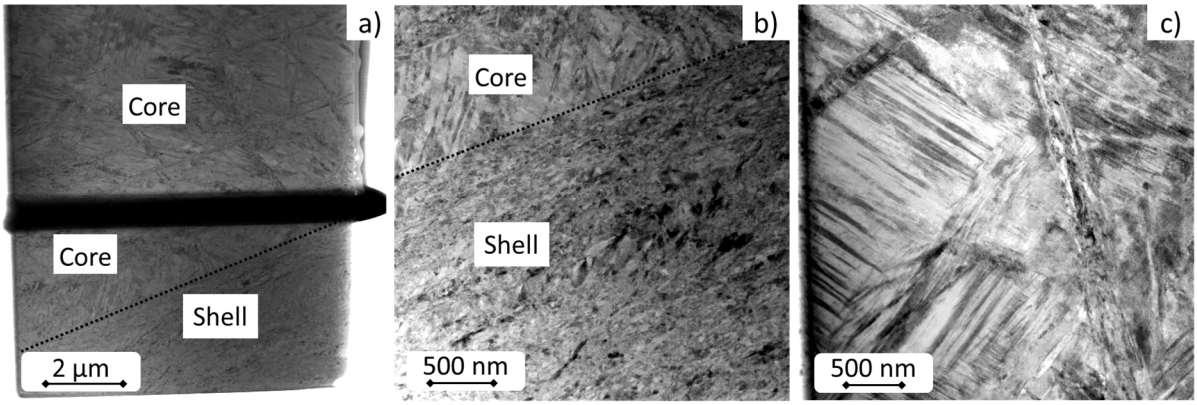

Fig. 5. TEM observations on the MM powder a) thin foil revealing shell and core structure b) detail of the core and shell transition region, c) detail of the core structure

3.2 Characterization of IP-SPS and MM-SPS specimens

HEXRD characterizations of IP-SPS and MM-SPS specimens revealed that specimens consisted of a mixture of α and β phases. The α phase fraction in IP-SPS and MM-SPS obtained from Rietveld refinement was 62 and 65 wt.%, respectively. The α phase fraction was also measured by quantitative image analysis of SEM-BSE micrographs; the content varied between 63 and 65 wt.%. These values are consistent with the one obtained by Angelier et al [33] (59%) for a cooling from 820 °C with a rate of 600 °C/h. As the amounts of α phase are similar, no oxygen, carbon or nitrogen contamination during the milling and SPS processes is expected. In order to confirm this assumption, the β transus temperature (T_β) of IP-SPS and MM-SPS specimens was characterized by electrical resistivity (ρ). Variations in electrical resistivity were measured during heating up to 1100 °C, at 2 °C/min. The normalized change of the electrical resistivity ($\Delta\rho/\rho_0$, where ρ_0 is the electrical resistivity at room

temperature) is plotted versus temperature **Fig. 6**. Between 200 °C and 650 °C, slight changes in $\Delta\rho/\rho_0$ are observed. Between 650 °C and 895 °C, a significant decrease of $\Delta\rho/\rho_0$ is measured, associated with the decrease of α phase amount [34]. The further increase above 895 °C corresponds to the variation of electrical resistivity associated with the temperature increase. For both experiments, the change in behavior occurs near 895 °C estimated as T_β. That value is similar to T_β of the initial material [24]. We can thus consider that powders and SPS specimens do not present any effect of contamination.

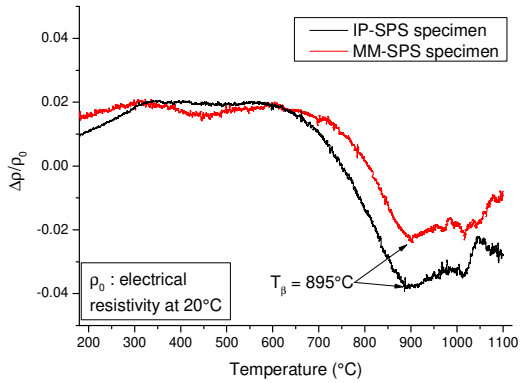

Fig. 6. Normalized electrical resistivity versus temperature. β-transus temperature determination during continuous heating at 2°C/min

The microstructure of IP-SPS and MM-SPS specimens are shown in **Fig. 7**. Concerning the IP-SPS specimen, **Fig. 7a**, a nearly uniform morphology of α grains is observed with a homogeneous spatial distribution. Nevertheless, for the MM-SPS specimen, **Fig. 7b** and **Fig. 7c** two different morphologies are observed with α grains having either a lamellar morphology or a globular/nodular morphology. The areas with lamellar α grains can be viewed as separate islands ("Core") in the sea of nodular α grains ("Shell"). Such a microstructural network with bimodal grain size distribution where globular grains are surrounding lamellar ones can be termed as a ''Harmonic structure'', **Fig. 7c**.

The measured dimensions of α grains are shown in **Table 2**. For the IP-SPS specimen, some grains could only be characterized by one dimension, the equivalent mean diameter, equal to 2.2 µm. For other grains, the length and width were characterized. The mean values obtained are 0.8 µm and 3 µm respectively, leading to a shape factor of 0.27. It can be noticed that the equivalent mean diameter for the first set of grains is closed to the mean length for the second set (if we take account of error bars). Thus, the differences between the two sets of data are due to different cross-sections of the lamellae. We can thus confirm that we have one uniform population of α grains with a lamellar morphology. For the MM-SPS specimen, values are significantly different. Indeed, the nodular grains have an equivalent mean diameter equal to 3.5 µm and the lamellar grains have a mean width is 0.3 µm and their mean length 12.1 µm. The resulting shape factor of lamellae is 0.02. From those differences, we can expect differences in the transformation sequences. The transformation kinetics of IP and MM powders was thus analyzed.

Table 2. α-grain size analysis of IP-SPS and MM-SPS specimens.

Grain Size	**α-nodular grains**	**α-lamellar grains**		
	Mean Diameter (µm)	Mean Length (µm)	Mean Width (µm)	Shape factor (Width/Length)
IP-SPS Specimen	2.2 ±0.5	3 ± 1.6	0.8 ± 0.3	0.27
MM-SPS Specimen	3.5 ±1.4 (Shell region)	12.1 ± 4.6 (Core region)	0.3 ± 0.2 (Core region)	0.02

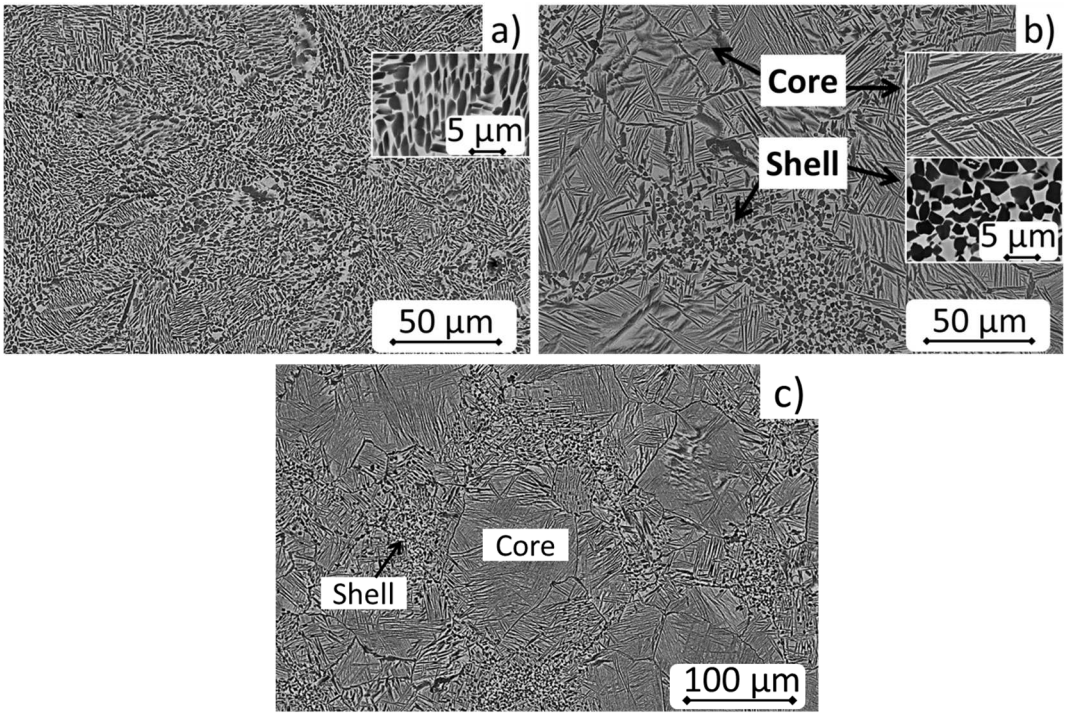

Fig. 7. The representative SEM-BSE micrographs of a) IP-SPS and b-c) MM-SPS Specimens

3.3 Transformation kinetics of IP powder during heat treatment

Transformation nature and kinetics for IP powders were obtained from in situ HEXRD experiment. Few selected diffractograms are given in **Fig. 8a** and the phase amounts versus temperature, determined by Rietveld refinement on all diffraction diagrams, are presented in **Fig. 8b**.

As shown in **Fig. 8a**, only the bcc β phase peaks can be observed at room temperature. During heating, no phase transformation could be revealed until 300 °C; above that temperature first phase formed is detected. As for similar studies [35-37], a base centred orthorhombic phase, called α''_{iso}[1] could be identified (**Fig. 8a** at 450 °C) with characteristic double peaks for 2θ angles near 3.1° and 5.4°. Its amount increases between 300 °C (5 wt%) and 530 °C (45 wt%) (**Fig. 8b**) and then slowly decreases. The characteristic double peaks of the orthorhombic structure evolve and tend toward single peaks corresponding to the HCP structure. This can be observed on diffractograms obtained at 530 °C and 650 °C, temperature for which diffraction peaks correspond to those of the HCP structure of the α phase (**Fig. 8a**) in addition to those of the matrix (β phase). As temperature increases, the amount of α phase decreases (**Fig. 8b**). At the end of the holding, the amount is equal to 26 wt%. The α phase fraction increases again during the continuous cooling at 0.23 °C/s until 500 °C, and then remains stable.

[1] It can be mentioned that other studies using TEM report the formation of a HCP α phase [38-40], and more recently the presence of an ordered face centered orthorhombic structure called O" [41]. Here, we consider the more commonly reported structure by using this technique [35][42] i.e., the base centered orthorhombic α''_{iso}, similarly to [21].

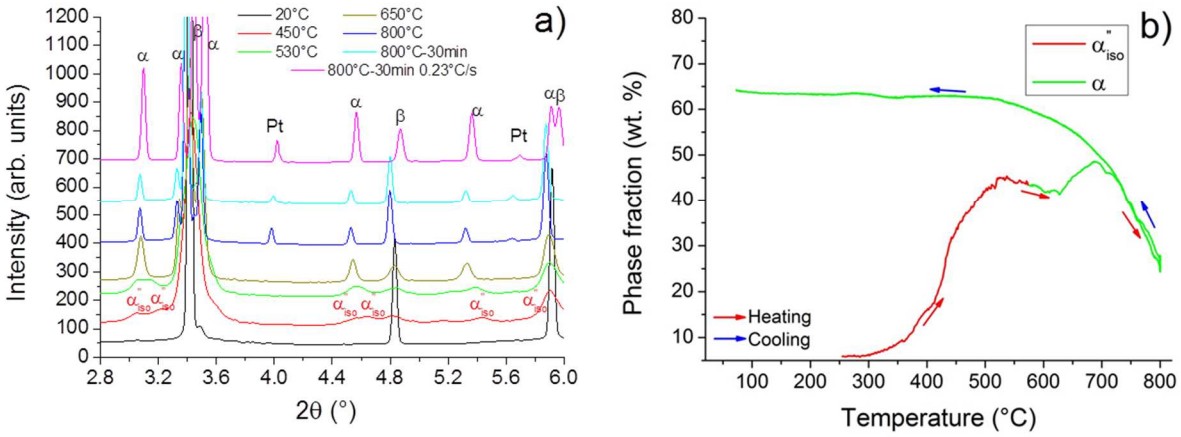

Fig. 8. a) HE XRD diffractograms b) α and α"$_{iso}$ phase fraction evolutions obtained by HEXRD (wt.%)

The microstructures obtained at different steps of the heat treatment are shown in **Fig. 9**. For all conditions, a mixture of α and β phase is observed, with α grains at the previous β/β grain boundaries and inside the parent β grain. For powders quenched at 600 °C, the microstructure is very thin (thickness near to 20 nm), **Fig 9a**. A very large density of intragranular α precipitates is observed, uniformly distributed in the β grains. For specimen quenched at 800 °C, the density of α precipitates and the amount are lower. The size of intragranular α grains increased and is near 500 nm, **Fig 9b**. Moreover, α_{GB} layers with a Precipitate Free Zone (PFZ) are observed at the previous β/β grains. For specimen quenched after holding 30 min at 800 °C (**Fig 9c**), the width of α_{GB} layers and the mean size of intragranular precipitates increases. Similar observations were reported in [38], and were associated with a coarsening of α precipitates during the heating stage and the dwell. At least, for specimen, heated up to 800°C, maintained 30 min and slowly cooled, the amount of α phase increases significantly. The width of α_{GB} layers remains nearly the same. However, the mean size of α intragranular precipitates increases (**Fig. 9d**). The PFZs are less marked.

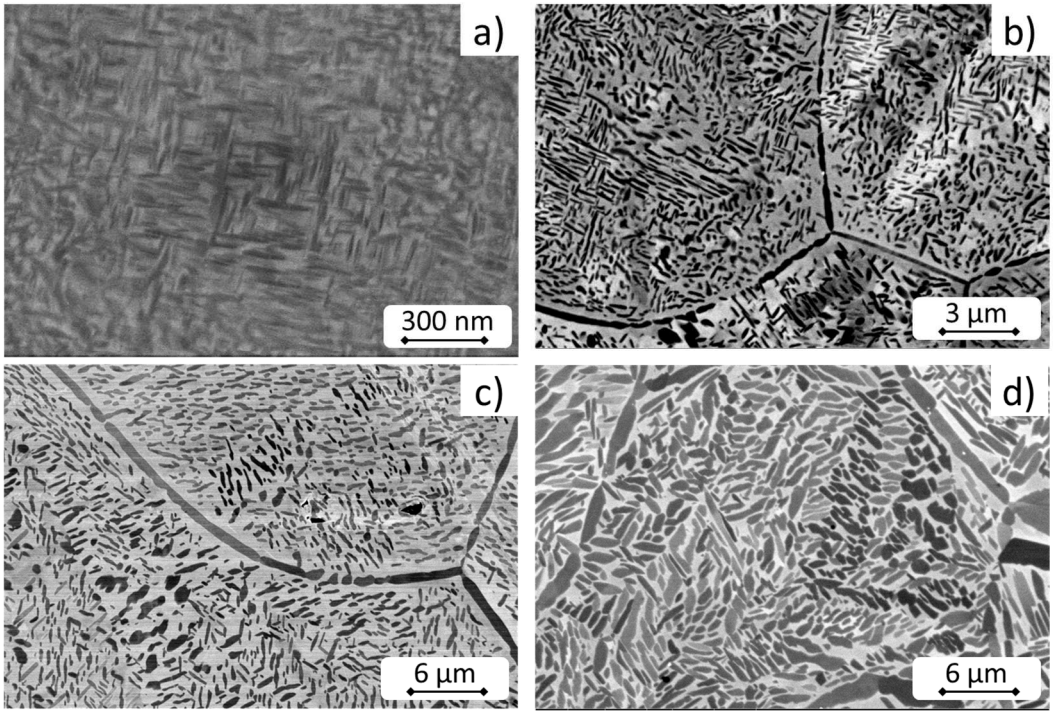

Fig. 9. SEM-BSE micrographs of IP powder at different stages: a) heated up to 600 °C b) heated up to 800 °C c) heated up to 800 °C + holding 30 minutes and quenched d) similar to SPS thermal path.

The very fine microstructure observed at 600 °C can be associated with the formation of metastable phases on heating at the lower temperatures (ω_{iso} for example [39] or α" [35-37]). Formation of α" between 300°C and 500°C was characterized by HEXRD. But it could not highlight neither the presence of ω_{ath} nor the formation of ω_{iso}. As electrical resistivity is very sensitive to phase transformation [43], in situ electrical resistivity measurements were realized on dense specimens in order to highlight any possible formation of ω phase for the heating rate considered. A dense IP-SPS specimen was used, which was first heat-treated in the β domain at 920 °C and further quenched by helium gas to RT to obtain a β-metastable state (as for the IP powders, **Fig. 10**). The electrical resistivity variations were measures (four point's method) during the heat treatment with conditions shown in **Fig. 1b**.

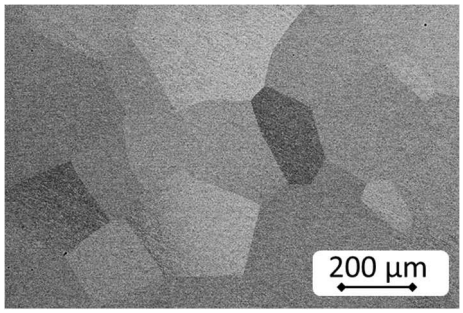

Fig. 10. Microstructures of β solution treated IP-SPS specimen

Variations in electrical resistivity (normalized by the electrical resistivity at room temperature) versus temperature are shown in **Fig. 11**. A decrease in electrical resistivity ($\Delta\rho/\rho_0$) is first measured at the beginning of the heating, from room temperature to about 190 °C, which is usually attributed to the vanishing of ω_{ath} phase [44-45]. Between 190 °C and about 300 °C, a change in slope is detected. Following the results of the literature [39][46], it is associated with the formation of ω_{iso} phase. This behavior is similar to that obtained for other β-metastable alloys transformed on heating from the β metastable state [38][44].

From 310 °C to 385 °C the electrical resistivity increases with temperature. This domain is associated with the evolution of ω_{iso} phase, and the formation of other nanosized precipitates that were identified either as a base centered orthorhombic phase ($\alpha"_{iso}$) or by the HCP α phase. It corresponds to the formation of $\alpha"_{iso}$ observed by HEXRD.

From 385 °C to 580 °C, the electrical resistivity decreases. This decrease can be associated with the evolution of the $\alpha"_{iso}$ phase, where the precipitate sizes increase and the interface number with the β phase decrease. Due to the very low size of these precipitates, the role played by the interfaces on the electrical resistivity signal is important [45]. Then, a decrease of electrical resistivity can be observed during the $\alpha"_{iso}$ phase fraction increase.

From 580 °C, a change of slope is observed. It can be attributed to the evolution of the $\alpha"_{iso}/\alpha$ phases, which structure evolves toward the HCP structure of the α phase (**Fig. 8a**) and which amount decreases as temperature increases (**Fig. 8b**).

The variation in electrical resistivity during the slow cooling (0.23 °C/s) to room temperature is also shown in **Fig. 11**. The continuous increase in electrical resistivity between 800 °C and 500 °C indicates the further growth of α precipitates. This behavior is consistent with HEXRD results (**Fig. 8b**) and is the one expected considering the cooling rate and the amount of equilibrium a phase with temperature [33].

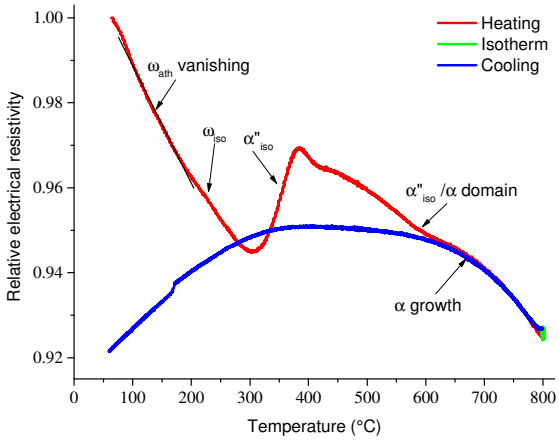

Fig. 11: Electrical resistivity answer during similar SPS thermal treatment on IP-specimen

Electrical resistivity experiments on dense IP-SPS samples evidence the formation of ω_{iso} phase for the heating condition used. Thus, a similar behavior is expected for IP powders. Combining HEXRD and electrical resistivity results it can be concluded that the decomposition of the β metastable phase of the β-CEZ alloy, during continuous heating, consisted of the following sequence of phase transformation:

$$\omega_{ath} + \beta \xrightarrow{up\ to\ 190\ °C} \omega_{iso} + \beta \xrightarrow{up\ to\ 310\ °C} \alpha''_{iso} + \beta \xrightarrow{up\ to\ 580\ °C} \alpha + \beta$$

3.4 Transformation kinetics in mechanically milled powder

Transformation nature and kinetics for MM powders were obtained from HEXRD experiment. A few diffractograms are given in **Fig. 12a** and the phase amounts versus temperature determined by Rietveld refinement are presented in **Fig. 12b**. At room temperature, the MM powder consists of 73 wt.% strain-induced martensite α" (centered orthorhombic structure). During the heating, the diffraction peaks of the orthorhombic base-centered structure are still present. Their intensity slightly decreases and their positions evolve up to about 590 °C and tend toward the peak position of the α phase (HCP structure). For example, the peaks (110)α" and (020)α" tend toward the peak (100)α. We thus consider that the α" phase (orthorhombic base-centered structure) evolves continuously toward the α phase. Changes in lattice parameters observed are due to changes in the temperature and in the chemical composition of the α" phase. In order to quantify the phase amounts, using Rietveld analysis, we have considered a mixture of α"+β phases at temperatures lower than 590 °C and a mixture of α+β phases above 590 °C. At 590 °C about 58 wt.% of α is measured. From 690 °C to 800 °C, the fraction of α phase sharply decreases as for IP specimen, and it remains nearly constant during the holding. During the cooling, the fraction of α increases while that the fraction of β decreases. No other phase was evidenced.

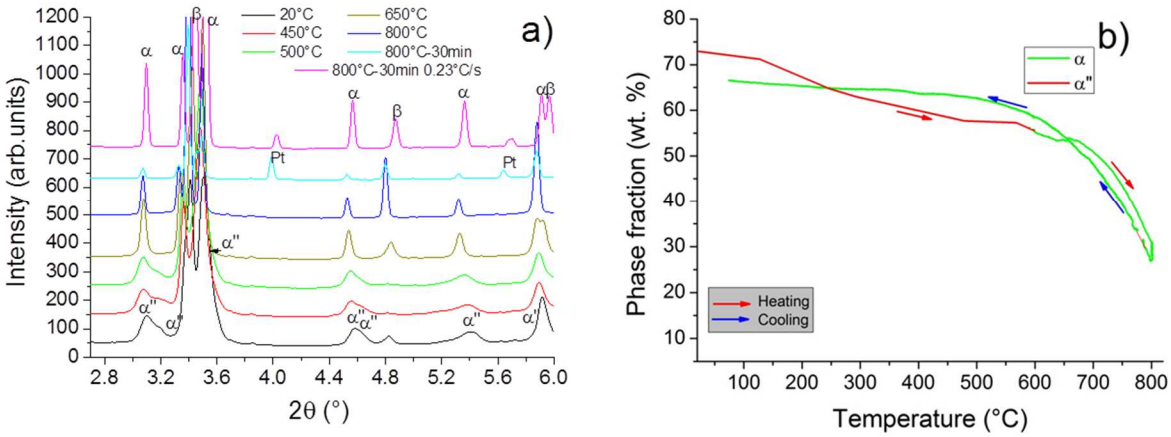

Fig. 12. The behavior of MM-powder during "SPS thermal path": a) HEXRD diffractograms during heating b) Phase fraction evolution during heating and cooling.

The microstructures obtained at different steps of the heat treatment are shown in **Fig. 13**. At 450 °C, the thin plates of "martensite" are still present (**Fig. 13a**), and even more easily evidenced compared to those observed at room temperature (**Fig. 4b**). Micro-segregations are also evidenced. At the end of the heating, the microstructure exhibits very thin α grains (**Fig. 13b**). Some differences can be noticed with α precipitates having a more lamellar shape in the core and a more nodular one in the shell. After 30 min holding at 800 °C (**Fig. 13c**), a change in α morphology is observed. SEM-BSE micrographs are more contrasted and highlight the nodular morphology in the powder shell and the lamellar morphology in the powder core; a coarsening of the precipitates can also be noticed. After the slow cooling to room temperature, the density of α precipitates does not change significantly, however their mean size increases, indicating that growth of the α precipitates occurs. For the lamellar precipitates, the growth seems more effective in the width, while nodular precipitates seem to grow homothetically (**Fig. 13d**). The lamellar α precipitates are homogeneously distributed in the β grains, with a well-defined orientation that can be considered as inherited from the α" laths orientation.

After the thermal treatment, the amount of α phase for MM powder is comparable to that in the IP powder. However, the transformation sequence is different. During the continuous heating, the following sequence of phase transformation occurs:

$$\alpha''_{stress-induced} + \beta \xrightarrow{up\ to\ 590\ °C} \alpha + \beta$$

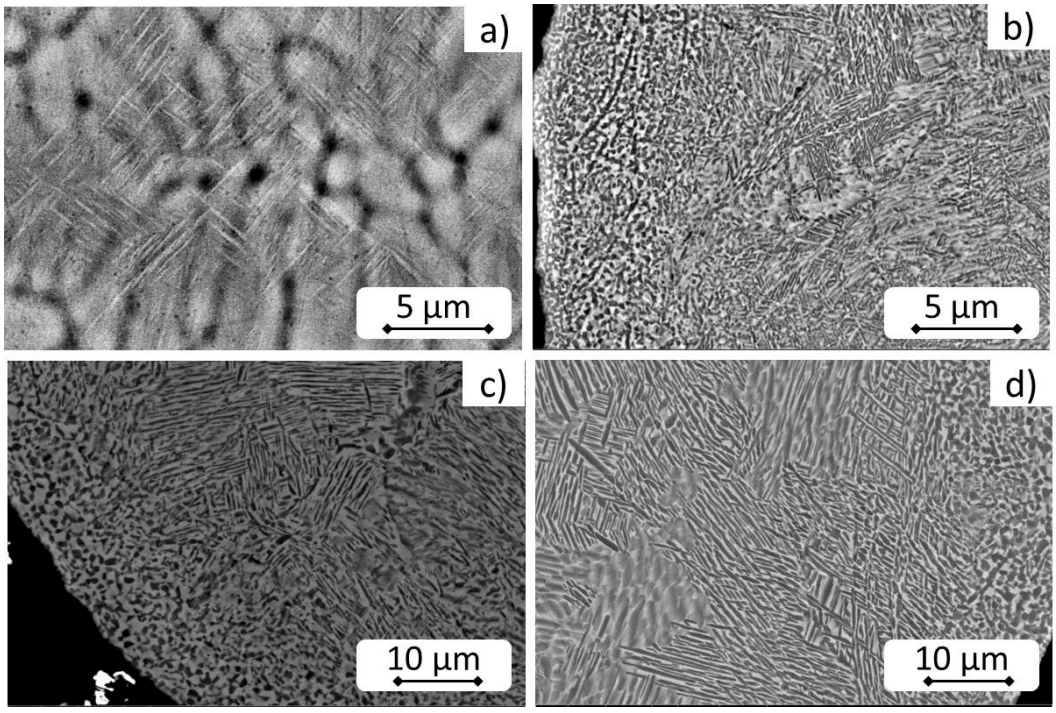

Fig. 13. SEM-BSE micrographs of MM powder at different stages: a) heated to 450 °C b) heated to 800 °C c) heated to 800 °C, hold for 30 minutes and quenched d) similar to SPS thermal path.

In addition, the similarity between the harmonic microstructure obtained on the MM-SPS specimen and the microstructure in the MM powder after heat treatment is evidenced in **Fig. 14** with a globular morphology in the shell and a lamellar one in the core. It can be predicted that the powder particles of two or more adjacent MM powder particles combine and form a continuous network of shell areas after SPS, **Fig. 7c**.

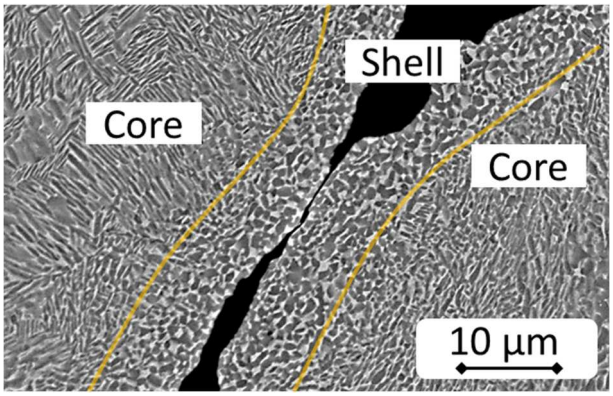

Fig. 14. Formation of a harmonic microstructure a) after SPS b) for two powder grains

In order to understand the development of α nodular grains in the powder shell, EBSD analysis was realized in the core and the shell of MM powder thermally treated similarly to SPS process. In the powder core, the IPF β map **(Fig. 15b)** evidences one main color, corresponding to single orientation of β matrix. This was confirmed by misorientation measurements in the β phase. The cumulative relative frequency of β misorientation in the core (subset 1) show that 92 % of the β domains have a misorientation angle below 5° and 100 % have a misorientation lower than 8° (**Fig. 15c**). In the same area, the IPF α map reveals several clusters of α lamellae with the same variant (**Fig. 15a**). The clusters' size is about 5 to 10 µm. Considering that α grains are inherited from strain-induced α", it can be concluded that these single α variant clusters are inherited from a group of single variant α" martensite plates, as shown in **Fig. 4b**. The α and β phases are in BOR [47], as shown in **Fig. 16a**.

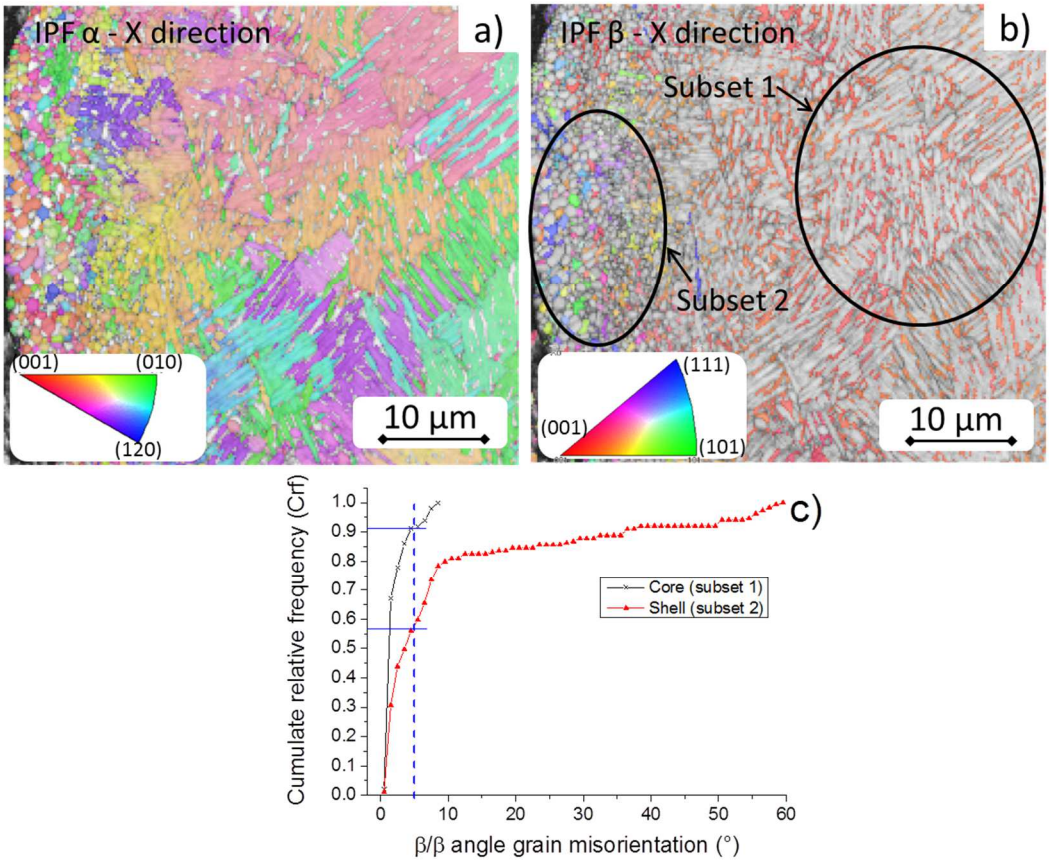

Fig. 15. EBSD on MM powders after SPS thermal path a) IPF α and b) IPF β maps with c) corresponding β/β misorientation.

EBSD analysis in the powder shell, reveals more differences in the crystallographic orientation of α and β grains (**Fig. 15**). The cumulative relative frequency of β misorientation in the shell characterized in subset 2, highlights that 43 % of β domains have a misorientation angle larger than 5° and 16 % of β domains have a misorientation angle larger than 15° (**Fig. 15c**). Pole figures (**Fig. 16**), show that the phases are still in BOR. However, a spread crystallographic orientation is observed **Fig. 16b**. The α grains are smaller (about 1µm) and nearly nodular. Many fine β domains (size of about 1 µm) are observed with different orientations. These results confirm the occurrence of recovery/recrystallization during the thermal treatment for both phases. It is evidenced by the rotation of crystallographic orientation of the initial larger β grain and the development of sub-grains and further little β grains as observed in [48]. For the α phase, the spread of crystallographic orientation in the shell is a characteristic feature of a recovery/recrystallization process [49-50].

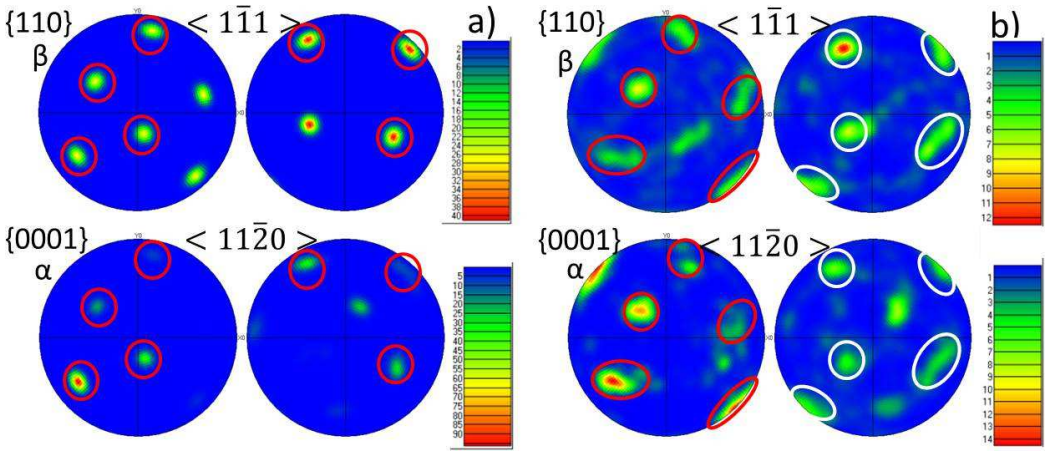

Fig. 16. Pole figures of IPF maps showing BOR between α and β on MM powders after similar SPS thermal path a) in the core and b) in the shell.

During the heating, recovery and dynamic recrystallization processes of the mixture α"/α+β must be involved to explain the changes in morphology. We can assume that the phenomena are similar to the formation of the globular α phase after forging at high temperature in the α+β temperature range [51-52]. In the present case the deformed initial martensite plates are partly dissolved during the heating, favoring grain boundary graving and α nodules formation [53].

Conclusion

We have investigated the formation of novel harmonic microstructure in a β-metastable alloy, the β-CEZ alloy. We set off with two different states; one is from as received PREP initial powder, and another one is obtained after mechanical milling of PREP powder. The spark plasma sintering of both powders under similar conditions produces a mixture of α+β phases with a similar fraction of α phase. However, the spatial distribution and morphology of α phase are completely different. Without mechanical milling, the morphology of α phase is lamellar and uniform in all volume. Concerning the sample got from mechanically milled powder, we observe an α network-type arrangement in the β matrix named "Harmonic Structure" with nodular α grains in the shell and lamellar α grains in the core. High-energy X-ray diffraction measurements with stepwise microstructural characterization (SEM and EBSD) revealed the influence of the initial state of powders on the precipitation sequence and the spatial distribution of α phase.

From the β-metastable state of the initial powder, the development of this unique arrangement of grains with different morphology can be explained by the following successive stages:

- Mechanical milling at room temperature implying large strain-induced martensite formation in the powder core and shell;
- Mechanical milling also implies a large plastic deformation of the powder particles at the surface (in the α" and β mixture) within a depth of about 7 µm (**Fig. 4d**);
- During the heating at $T < T_\beta$, α" structure evolves toward the HCP α structure;
- In the powder particles shell, the spread of crystallographic orientation evidences recovery and recrystallization giving small α and β grains with size below 1 µm;
- In the powder particles core, the α lamellae keep a low shape factor (width/length) inherited from the α" morphology. Moreover, each α variant inherits the orientation of the stress/strain α" variant keeping the variant selection that occurred during the milling; it implies that no recovery/recrystallization occurred;
- During the SPS process, the powder particles are sintered together, producing specimens constituted of periodic "core" of α lamellae surrounded by a continuously connected network of fine-grained "shell" of α nodular grains.

Acknowledgment

This work was supported by the French National Research Agency, in the framework of ANR 14-CE07-0003 “HighS-Ti” program and through the program “Investment in the future” referenced by Labex DAMAS ANR-11-LABX-0008-01. We thank the support by the Japan Society for the Promotion of Science (JSPS) and their Grant-in-Aid for Scientific Research JP18H05256 and JP18K18962. The authors gratefully acknowledge the European Synchrotron Radiation Facility (ESRF) for the provision of beam time at beamline ID15A. We thank the LEM3 laboratory and especially Yudong Zhang for EBSD map (**Fig. 15** and **Fig. 16**). We thank also Stéphanie Bruyère at IJL laboratory to TEM observations (**Fig. 5**).

Reference

[1] G. Lütjering, J.C. Williams. Titanium, second ed., Springer, Berlin (2007) ISBN 978-3-540-71397-5.

[2] R.R. Boyer. Material Science and Engineering, **213**, 1-2 (1996) 103-114. doi:10.1016/0921-5093(96)10233-1

[3] M. Niinomi, C.J. Boehlert. Advances in Metallic Biomaterials, Springer chap. **8** (2015) 179-213. doi:10.1007/978-3-662-46836-4

[4] J. D. Cotton, R.D. Briggs, R.R. Boyer, S. Tamirisakandala, P. Russo, N. Shchetnikov, J.C. Fanning. JOM **67**, No. 6 (2015) 1281-1303. doi:10.1007/s11837-015-1442-4

[5] B. Jiang, S. Emura, K. Tsuchiya. Material Science and Engineering A, **722** (2018) 129-135. doi:10.1016/j.msea.2018.03.025

[6] Y. Estrin, A. Vinogradov. Acta Materialia **61** (2013) 782-817. doi:10.1016/j.actamat.2012.10.038

[7] X. Sauvage, G. Wilde, S.V. Divinski, Z. Horitac, R.Z. Valiev. Material Science and Engineering A **540** (2012) 1-12. doi:10.1016/j.msea.2012.01.080

[8] H. Jin, D. J. Lloyd. Scripta Materialia **50** (2004) 1319–1323. doi:10.1016/j.scriptamat.2004.02.021

[9] B. Srinivasarao, K. Oh-ishi, T. Ohkubo, T.Mukai, K.Hono. Scripta Materialia, **58**, 9 (2008) 759-762. doi:10.1016/j.scriptamat.2007.12.016

[10] S.K. Vajpai, C. Sawangrat, O. Yamaguchi, O.P. Ciuca, K. Ameyama. Material Science and Engineering C, **58** (2016) 1008–1015. doi:10.1016/j.msec.2015.09.055

[11] S.K. Vajpai, M. Ota, T. Watanabe, K. Ameyama. Metallurgical and Materials Transactions A **46** (2015) 903-914. doi:10.1007/s11661-014-2649-7

[12] Z. Zhang, S.K. Vajpai, D. Orlov, K. Ameyama. Material Science and Engineering A, **598** (2014) 106–113. doi:10.1016/j.msea.2014.01.023

[13] T. Sekiguchi, K. Ono, H. Fujiwara, K. Ameyama. Materials Transactions **51** (2010) 39–45. doi:10.2320/matertrans.MB200913

[14] S. K. Vajpai, K. Ameyama. Intermetallics, **42** (2013) 146-155. doi:10.1016/j.intermet.2013.06.006

[15] T. Sekiguchi, NBR Sabrina, R. Imao, H. Fujiwara, K. Ameyama, ZH Zhao, A. Ueno. Ti-2011: Proceedings of the 12th world conference on titanium, Edited by, Lian ZHOU, , Hui CHANG, Yafeng LU, Dongsheng XU, 2012 Science Press Beijing, Vol. 2, 998-1001.

[16] S.K. Vajpai, K. Ameyama, M. Ota, T. Watanabe, R. Maeda, T. Sekiguchi, G. Dirras, D. Tingaud, IOP Conference Series: Material Science and Engineering, **63** (2014) doi:10.1088/1757-899X/63/1/012030.

[17] G. Dirras, D. Ueda, A. Hocini, D. Tingaud, K. Ameyama. Scripta Materialia **138** (2017) 44-47. doi:10.1016/j.scriptamat.2017.05.033

[18] G. Dirras, D. Tingaud, D. Ueda, A. Hocini, K. Ameyama. Materials Letters, **206** (2017) 214-216. doi:10.1016/j.matlet.2017.07.027

[19] T. Grosdidier, M.J. Philippe. Materials Science and Engineering A **291** (2000) 218–223. doi: 10.1016/S0921-5093(00)00921-7

[20] J.D.C. Teixeira, B. Appolaire, E. Aeby-Gautier, S. Denis, G. Cailletaud, N. Spath. Materials Science and Engineering A, **448**, 1-2 (2007) 135-145. doi:10.1016/j.msea.2006.10.024

[21] N. Maury, B. Denand, M. Dehmas, C. Archambeau-Mirguet, J. Delfosse, E. Aeby-Gautier. Journal of Alloys and Compounds, **763** (2018) 446-458. doi:10.1016/j.jallcom.2018.04.302

[22] M. Tokizane, T. Fukam, T. Inaba. ISIJ International, **31**, No. 10 (1991) 1088-1092. doi:10.2355/isijinternational.31.1088

[23] K. Isonishi, M. Tokizane. ISIJ International, **76**, No. 12 (1990) 2108-2115. doi:10.2320/jinstmet.J2016008

[24] J.O. Peters G. Lutjering, M. Koren, H. Puschnik , R.R. Boyer. Materials Science and Engineering A **217** (1995) 71-80. doi:10.1016/0921-5093(96)10225-2

[25] L. Ropars, M. Dehmas, S. Gourdet, J. Delfosse, D. Tricker, E. Aeby-Gautier. Journal of Alloys and Compounds **624** (2015) 179-188. doi:10.1016/j.jallcom.2014.10.203

[26] G. Geandier, E. Aeby-Gautier, A. Settefrati, M. Dehmas, B. Appolaire. C.R. Physique **13** (2012) 257–267. doi:10.1016/j.crhy.2011.12.001
[27] J. Kieffer, D. Karkoulis. PyFAI, Journal of Physics: Conference Series, IOP Publishing, **425** (2013) 202012 doi:10.1088/1742-6596/425/20/202012.
[28] H.M. Rietveld. Journal of Applied Crystallography 2 (1969) 65-71. doi:0.1107/S0021889869006558
[29] B. Denand, M. Dehmas, E. Aeby-Gautier, C. Bonnet, G. Geandier, J-P. Sarteaux, International patent deposed with reference number: WO2019081266A1, Four d'analyse portable pour ligne de rayonnement (available at https://patents.google.com/patent/WO2019081266A1/en)
[30] P. Archambault, D. Godard. Scripta Materialia **42** (2000) 675– 680 doi:10.1016/S1359-6462(99)00419-4
[31] T. Grosdidier, C . Roubaud, M-J. Philippe, Y. Combres. Scripta Materialia, **36**, No. 1 (1997) 21-28. doi:10.1016/S1359-6462(96)00341-7
[32] T. He, Y. Feng, W. Luo, Y. He, L. Tian, Y. Lai. Materials Characterization **138** (2018) 19–25 doi:10.1016/j.matchar.2018.01.056
[33] C. Angelier, J. Béchet. Journal de Physique IV Colloque, **04** (1994) C3, 111-116. doi:10.1051/jp4:1994315
[34] F. Bruneseaux, E. Aeby-Gautier, G. Geandier, J. Da Costa Teixeira, B. Appolaire, P. Weisbecker, A. Mauro. Materials Science and Engineering A **476** (2008) 60–68 doi:10.1016/j.msea.2007.04.072
[35] P. Barriobero-Vila, G. Requena, S. Schwarz, F. Warchomicka, T. Buslaps. Acta Materialia **95** (2015) 90-101. doi:10.1016/j.actamat.2015.05.008
[36] A. Settefrati, E. Aeby-Gautier, M. Dehmas, G. Geandier, B. Appolaire, S. Audion, and J. Delfosse. Solid State Phenomena, **172-174** (2011) 760-765. doi:10.4028/www.scientific.net/SSP.172-174.760
[37] E. Aeby-Gautier, A. Settefrati, F. Bruneseaux, B. Appolaire, B. Denand, M. Dehmas, G. Geandier, P. Boulet. Journal of Alloys and Compounds, **577**S (2013) S439–S443 doi:10.1016/j.jallcom.2012.02.046.
[38] R. Sanguinetti, M. Zandona, A. Pianelli, E. Aeby-Gautier. Journal de Physique IV, **4** (1994) 99-104. doi :10.1051/jp4:1993785
[39] S. Nag, R. Banerjee, R. Srinivasan, J.Y. Hwang, M. Harper, H.L. Fraser. Acta Materialia **57** (2009) 2136–2147. doi:10.1016/j.actamat.2009.01.007
[40] F. Prima, P. Vermaut, G. Texier, D. Ansel, T. Gloriant. Scripta Materialia **54** (2006) 645–648 doi:10.1016/j.scriptamat.2005.10.024
[41] Y. Zheng, R.E.A. Williams, H.L. Fraser. Scripta Materialia **113** (2016) 202-205. doi: 10.1016/j.scriptamat.2016.01.024
[42] H. Chang, E. Aeby-Gautier, L. Zhou, Chin. Science Bulletin **59** 15 (2014) 1773-1777. doi :10.1007/s11434-014-0210-0
[43] U. Bohnenkamp, R. Sandstrom. Journal of Applied Physics **92** 8 (2002) 4402-4407 doi:10.1063/1.1502182
[44] J.C. Ho, E. W. Collings. Physical Review B **6** (1972) 3727-3738. doi:10.1103/PhysRevB.6.3727
[45] P. Zhanal, P. Harcuba, J. Smilauerova, J. Strsky, M. Janecek, B. Smola, M. Hajek. Acta Physica Polonica A, **128** (2015) 779-782. doi:10.12693/APhysPolA.128.779
[46] T. Li, D. Kent, G. Sha, L. T. Stephenson, A. V. Ceguerra, S. P. Ringer, M. S. Dargush, J. M. Carnei. Acta Materialia **106** (2016) 353-366. doi:10.1016/j.actamat.2015.12.046
[47] W.G. Burgers. Physica, **1** Issues 7-12 (1934) 561–586 doi:10.1016/S0031-8914(34)80244-3.
[48] D. Qin, D. Guo, L. Zheng, Y. Li. Journal of Alloys and Compounds, **769** (2018) 725-731. doi:10.1016/j.jallcom.2018.08.053
[49] A. Bhattacharyya, E. El-Danaf, S.R. Kalidindi, R.D. Doherty. International Journal of Plasticity **17** (2001) 861-883 doi:10.1016/S0749-6419(00)00072-3
[50] T.R. Bieler, S.L. Semiatin. International Journal of Plasticity **18** (2002) 1165-1189 doi:10.1016/S0749-6419(01)00057-2

[51] I. Weiss, F.H. Froes, D. Eylon, G.E. Welsch. Metall Mater Trans A **17** (1986) 1935–1947 doi:10.1007/BF02644991.
[52] D. Banerjee, J.C. Williams. Acta Materialia **61** (2013) 844–879. doi:10.1016/j.actamat.2012.10.043
[53] O.M. Ivasishin, P.E. Markovsky, Y.V. Matviychuk, S.L. Semiatin. Metallurgical and Materials Transactions A **34** (2003) 147–158. doi:10.1007/s11661-003-0216-8